Atmos. Chem. Phys. Discuss., 11, 26477–26520, 2011
www.atmos-chem-phys-discuss.net/11/26477/2011/
doi:10.5194/acpd-11-26477-2011

Atmospheric Chemistry and Physics Discussions

Simulation of mineral dust aerosol with piecewise log-normal approximation (PLA) in CanAM4-PAM

Y. Peng[1], **K. von Salzen**[2], **and J. Li**[2]

[1]Canadian Centre for Climate Modelling and Analysis, School of Earth and Ocean Sciences, University of Victoria, Victoria, BC, V8W 3P6, Canada
[2]Canadian Centre for Climate Modelling and Analysis, Environment Canada, Victoria, BC, V8W 3P6, Canada

Received: 29 August 2011 – Accepted: 5 September 2011 – Published: 22 September 2011

Correspondence to: Y. Peng (yiran.peng@ec.gc.ca)

Published by Copernicus Publications on behalf of the European Geosciences Union.

Abstract

A new size-resolved dust scheme based on the numerical method of piecewise log-normal approximation (PLA) was developed and implemented in the fourth generation of the Canadian Atmospheric Global Climate Model with the PLA Aerosol Module (CanAM4-PAM). The total simulated annual mean dust burden is 37.8 mg m^{-2} for year 2000, which is consistent with estimates from other models. Results from simulations are compared with multiple surface measurements near and away from dust source regions, validating the generation, transport and deposition of dust in the model. Most discrepancies between model results and surface measurements are due to unresolved aerosol processes. Radiative properties of dust aerosol are derived from approximated parameters in two size modes using Mie theory. The simulated aerosol optical depth (AOD) is compared with several satellite observations and shows good agreements. The model yields a dust AOD of 0.042 and total AOD of 0.126 for the year 2000. The simulated aerosol direct radiative forcings (ADRF) of dust and total aerosol over ocean are −1.24 W m^{-2} and −4.76 W m^{-2} respectively, which show good consistency with satellite estimates for the year 2001.

1 Introduction

Mineral dust aerosol is one of the important contributors to global aerosol loading and radiative forcing (Textor et al., 2006), originating from aeolian erosion in arid and semi-arid regions, going through complex atmospheric processes and exerting strong impacts on regional and global climates (Solomon et al., 2007).

Dust aerosols absorb and scatter both solar and terrestrial radiation. However, the direct radiative forcing of dust is still quite uncertain. Even the sign of this forcing is under debate. Most uncertainties are attributed to the calculation of optical properties, which are dependent upon the simulated dust fraction in different size modes (e.g., Kinne et al., 2006; Schulz et al., 2006). The vertical distribution of dust is also an

ACPD
11, 26477–26520, 2011

uncertain factor for estimation of longwave radiative forcing (Solomon et al., 2007).

Dust aerosols may act as cloud condensation nuclei (CCN) if coated with soluble aerosols (such as sulfate), and affect cloud droplet number and size, thus inhibiting precipitation (e.g., Rosenfeld et al., 2001). Dust is also an efficient ice nucleus (IN) (Sassen, 2002) and may have diverse effects in mesoscale cloud systems by changing cloud properties under different temperature and humidity conditions (Min et al., 2009). Additionally, dust aerosols are a source of iron, which, once deposited, affects marine biogeochemical processes that contribute to the uptake of carbon by the ocean (Jickells et al., 2005).

Global climate models (GCMs) have been used in several studies for simulation of the global dust cycle. By applying bulk microphysics of atmospheric aerosols (e.g., only the total number or/and mass of aerosols are traced through modelled processes), the first-order pattern of the dust distribution can be reproduced (e.g., Tegen and Fung, 1994; Reader et al., 1999). Huneeus et al. (2011) conducts a multi-parameter and multi-model intercomparison of global dust models, and suggests that size-resolved information is a significant factor in improving the dust simulation. Both bin and modal methods have been introduced in recent GCMs to simulate size-segregated emission and transport processes of dust aerosol (e.g., Gong et al., 2003; Stier et al., 2005). However, model results still exhibit large variations. The simulated dust annual emission flux ranges between 1000 and 3000 $\mathrm{Tg\,yr^{-1}}$ in different GCMs (Zender et al., 2004). An estimate of dust dry mass column burden from AeroCom (Aerosol Comparisons between Observations and Models) provides a median value of 39.1 $\mathrm{mg\,m^{-2}}$ with a range from 8.8 to 57.8 $\mathrm{mg\,m^{-2}}$ (Textor et al., 2006). The simulated optical depth of dust aerosol is between 0.009 and 0.054, with a median of 0.032 from AeroCom (Kinne et al., 2006). Solomon et al. (2007) summarized dust direct radiative effects from several recent models, which range from −0.56 to +0.1 $\mathrm{W\,m^{-2}}$.

Both dust aerosol distribution and radiative forcing are not well quantified due to limited understanding of fundamental physical processes as well as sparse observations on a global scale. Dust concentrations from the network of the University of

ACPD
11, 26477–26520, 2011

Miami (Prospero, 1996) are often used for model validation. These in-situ data are climatologically representative but are only available for a small number of remote marine sites. AERONET (Aerosol Robotic Network) provides long-term measurements of aerosol optical properties with a global coverage (Dubovik et al., 2006). In addition, data extracted from AERONET and other sources are compiled and archived in the Dust Indicators and Records in Terrestrial and Marine Paleoenvironments (DIRTMAP) dataset (Kohfeld and Harrison, 2001) for deposition fluxes at numerous sites.

In recent decades, a global view of the aerosol distribution became available through satellite observations with passive remote sensors. For example, optical depth at 0.55 µm is a common product from MODIS (Moderate Resolution Imaging Spectroradiometer) and MISR (Multi-angle Imaging SpectroRadiometer) on board the NASA Terra platform (Kahn et al., 2005). However, such measurements still have limitations, e.g., MODIS data is mainly restricted to the ocean because large radiances from highly reflective land surface typically overwhelm those from aerosols (Kaufman et al., 2005).

Despite our limited understanding and restricted observations, the role of dust aerosol as one of the major components in the atmosphere and its non-negligible impacts on climate have been well established.

In this study, we extend the fourth generation of the Canadian Atmospheric Global Climate Model (CanAM4) to include a new representation of the dust cycle. The numerical method of Piecewise Log-normal Approximation (PLA) is applied to simulate the size distribution of dust aerosol particles (von Salzen, 2006). In Sect. 2, the model setup and application of the PLA approach to dust simulations are described. Model results are validated by comparing with surface measurements of the dust size distribution, mass concentration and deposition rates, as shown in Sect. 3. Optical properties of dust are also calculated and compared with satellite observations in Sect. 4. Conclusions of this study and relevant discussions are presented in Sect. 5.

ACPD
11, 26477–26520, 2011

2 Model description and PLA methodology

The fourth generation of the Canadian Atmospheric Global Climate Model (CanAM4) represents the starting point for the development of a comprehensive earth system model at CCCma (Canadian Centre for Climate Modelling and Analysis, von Salzen et al., 2005). In this study, a spectral resolution with the triangular truncation at wave number of 47 (T47) is employed, which roughly corresponds to a horizontal resolution of 3.75°×3.75°. Thirty-five vertical layers are used from the surface up to 1 hpa, with a resolution of about 100 m near the surface.

The Piecewise Log-normal Approximation (PLA) method (von Salzen, 2006) is used in CanAM4 to represent the aerosol size distribution. In the following, the newly created model will be referred to as CanAM4-PAM (PLA Aerosol Module).

It is recognized that bin and modal approaches are commonly used for size-resolved aerosol simulation in climate models. The PLA scheme takes advantage of both approaches by combining them into a hybrid method. The accuracy and computational efficiency of the PLA scheme have been demonstrated in von Salzen (2006). According to the PLA method, an aerosol number distribution can be expressed as:

$$n(\varphi) = \sum_i n_i(\varphi) \tag{1}$$

where φ is a dimensionless size parameter $\varphi \equiv \ln(R_p/R_0)$, R_p is the aerosol particle radius and R_0 is a reference radius of 1 μm.

In each section i, the aerosol number distribution is defined as:

$$n_i(\varphi) = n_{0,i}\exp[-\psi_i(\varphi-\varphi_{0,i})^2]H(\varphi-\varphi_{i-\frac{1}{2}})H(\varphi_{i+\frac{1}{2}}-\varphi) \tag{2}$$

where $n_{0,i}$, ψ_i and $\varphi_{0,i}$ are fitting parameters, representing the magnitude, width and location of the maximum of the distribution respectively. $H(x)$ is the Heaviside step function whose purpose is to constrain the log-normal distribution in each section to the particle size range between $\varphi_{i-\frac{1}{2}}$ and $\varphi_{i+\frac{1}{2}}$. In CanAM4-PAM, we prescribe the width

ACPD
11, 26477–26520, 2011

ψ_i. Fitting parameters $n_{0,i}$ and $\varphi_{0,i}$ and mass fractions for internally mixed types of aerosol are calculated at each model time step. These parameters are calculated from the integrated number (N_i) and mass (M_i) concentrations in each section (von Salzen, 2006). Both mass and number size distribution of dust particles are obtained through parameterization of physical processes in CanAM4-PAM. A more detailed description of the application to individual physical process is presented below.

2.1 Dust emissions

Dust aerosol originates from aeolian erosion in arid and semi-arid regions. A size-derived dust emission scheme (Marticorena and Bergametti, 1995; Marticorena et al., 1997) is used to provide an explicit representation of surface dust sources in CanAM4-PAM.

Emission of dust aerosols is not permitted in snow covered regions and vegetated areas over land in the model. The fractional dust source areas in the model grid cell is obtained from two off-line datasets. A potential dust source map is derived from a terrestrial biogeography model by including all non-forest biomes (Tegen et al., 2002), which is further combined with a global bare ground fraction dataset.

Dust emission is proportional to the bare ground fraction in CanAM4-PAM. Bare ground fraction over land is calculated offline in the Canadian Terrestrial Ecosystem Model (CTEM). CTEM (Arora and Boer, 2005) is a dynamic vegetation model, which includes nine plant function types (PFTs) such as trees, grass and crops. Areal fraction of CTEM PFTs are estimated with constraints derived from recent satellite observations. Bare ground fraction (F_{bg}) is obtained as one minus the sum of fractions of nine vegetation types:

$$F_{bg} = 1 - \sum_{k=1}^{9} \mathrm{PFT}_k \tag{3}$$

This approach allows for changes in the composition of natural vegetation and changes due to human activities, with conservation of total area of all PFTs in a model grid cell

ACPD
11, 26477–26520, 2011

(Wang et al., 2006). CTEM provides a global cover of vegetation and the bare ground fraction from 1850 to 2005, which is averaged over the 155-yr data to give a climatological dataset. The bare ground fraction is applied in combination with the potential dust source map to mask out the non-dusty area in CanAM4-PAM. Considering that the seasonality of vegetation cover is more predominant than its interannual variation, we prescribe 12 monthly means of derived bare ground fraction in CanAM4-PAM for this study. Figure 1 shows an average over these 12 monthly means of bare ground fraction in potential dust source regions.

Dust production is related to the motion of soil particles initiated by wind. The forces acting on particles include the weight, the interparticle cohesion forces, and the wind shear stress on the surface. The first two forces are dependent on the particle size as well as the soil moisture. The last force depends on the wind energy transferred to the erodible surface, which is controlled by the roughness elements on the surface (Marticorena and Bergametti, 1995). All forces together determine the minimum threshold friction velocity U^*_{th}, which is required to initiate the particle motion.

A threshold value (U^*_{th}) is obtained in combination with the surface roughness and soil moisture in the model. A global map of surface aerodynamic roughness length is obtained from an analysis of measurements with the European Remote Sensing (ERS) satellite scatterometer (Prigent et al., 2005; Cheng et al., 2008) and applied into the model as a climatological input field. Arid and semi-arid regions with high surface roughness require a large U^*_{th} to uplift soil particles. Because rough surface protects particles from the aeolian erosion, dust emission is inhibited.

As the soil moisture increases, soil water retention is responsible for the increase of the threshold wind friction velocity. Soil particles are adhesive to the surface in high moisture regions, thus dust emission is suppressed. Molecular adsorption on the soil particle surface as well as the capillary forces between particles are both taken into account. The influence of soil moisture on U^*_{th} is included in the model with a parameterization developed by Fécan et al. (1999). The soil moisture fraction in the parameterization is calculated in the Canadian Land Surface Scheme (CLASS) in

ACPD
11, 26477–26520, 2011

CanAM4-PAM (Verseghy, 1991). The wetter the soil is, the stronger the soil retention force and the U^*_{th} (Cheng et al., 2008).

Both surface roughness and soil moisture modify the threshold wind friction velocity, which indicates how much the soil properties and local conditions favor the uplift of erodible particles. The dust emission flux is essentially determined by the wind friction velocity (U^*), which is calculated as:

$$U^* \propto \sqrt{U_{10}^2 + U_{\text{gust}}^2} \tag{4}$$

where U_{10} and U_{gust} are wind speed at the height of 10 m and the gusty wind near the surface, respectively. Both wind components are predicted in model at each time step. Once $U^* > U^*_{th}$, the local wind stress is strong enough to overcome the particle weights and retention forces. The emitted flux of dust is proportional to U^{*3} (Marticorena and Bergametti, 1995). This power-dependence relation has been well-established and is applied in current climate models (e.g., Gong et al., 2003; Stier et al., 2005).

Twelve general soil types (Zobler, 1986) and five Asian soil types (Cheng et al., 2008) are considered in the model for the dust emission calculation. A global map of areal fraction for each soil type (A_{st}) is provided. Four soil populations of coarse sand, medium/fine sand, silt and clay are prescribed in four log-normal modes for each soil type. Compositional fractions of the four populations are also given for different soil types (Tegen et al., 2002). The soil particle radius (r) is obtained in 192 size bins within [0.05,55] µm according to the prescribed distribution and composition for each soil type (st). Thereafter the emitted dust mass flux at a certain particle size is given as:

$$D_e(r) \propto \sum_{\text{st}=1}^{17} U^{*3} f(R,w) A_{\text{st}} S_{\text{st}}(r) \tag{5}$$

where $f(R,w)$ denotes the influences of surface roughness (R) and soil moisture (w). $S_{\text{st}}(r)$ is the mass size distribution of each soil type.

ACPD
11, 26477–26520, 2011

After weighting with the bare ground fraction (F_{bg}), size-resolved mass fluxes of dust emission are integrated within two PLA sections. Particle radius in the first section is within [0.1,1] µm and within [1,10] µm in the second section.

$$M_1 = \int_{0.1}^{1} F_{bg} D_e(r) dr \qquad M_2 = \int_{1}^{10} F_{bg} D_e(r) dr. \tag{6}$$

Assuming spherical particles and a dust density of 2.65 g cm^{-3} globally, the number size distribution of emitted dust is available as well. Following Eq. (2), fitting parameters of the PLA size distribution can be derived from the calculated mass and number of the dust emission size distribution in each grid cell. The width parameter (ψ_i) in each PLA section is prescribed as 2.0.

The selection of size boundary and section width leads to a reasonable fit of PLA distribution to a global average of the emitted dust distribution (Fig. 2). With a climatological run of CanAM4, the annual global mean of emitted dust mass flux in 192 prescribed bins is shown in Fig. 2. Particles with radii larger than 10 µm are omitted in the PLA distribution, because these particles will fall back to the surface quickly with gravitational settling. This is consistent with observed evidence (e.g., Arimoto et al., 1997) that most atmospheric dust particles are smaller than several microns, even near the source regions. However, on a few occasions, giant aerosols with radii larger than 50 µm can be transported in the atmosphere. Considering that these giant particles have little radiative effect, we do not take them into account in this study.

2.2 Dust transport and deposition

For horizontal transport of mineral dust mass and number mixing ratios a spectral transform method is used, which is an extension of the hybrid variable transformation as described in Boer (1995). Unphysical negative values from spectral transport calculations are largely suppressed with the use of transformed variables (Merryfield et al., 2003), but the physical variable is not precisely conserved. A tracer mass correction method is therefore applied by assigning a scaling factor for simulated mass of each

ACPD
11, 26477–26520, 2011

tracer. The magnitude of the mass correction is proportional to the net tracer tendency resulting from all physical parameterizations in each grid cell.

The grid-cell mean continuity equation for dust in CanAM4-PAM is given by:

$$\frac{dM}{dt} = M_E - M_T - M_D - M_W \quad (7)$$

where M indicates the mass or number mixing ratio of dust aerosol in each of the PLA sections. $\frac{dM}{dt}$ is the tendency of mass or number mixing ratio. M_E represents dust emission, M_T is the transport by advection and vertical diffusion, M_D refers to dry deposition together with the gravitational settling. M_W refers to wet deposition by stratiform and convective clouds. The PLA distribution is obtained from the advected aerosol mass and number mixing ratios for each size section at each time step according to Eqs. (1) and (2).

As a major sink of dust aerosols, dry deposition together with gravitational settling accounts for about 80 % of dust removal globally (e.g., Textor et al., 2006). A size-dependent approach is used in this study. The dry deposition velocity is inversely proportional to a surface resistance, which is dependent on aerosol particle size as well as other properties of the surface and atmosphere (Zhang et al., 2001). The terminal velocity of gravitational settling is calculated as a function of aerosol particle radius, density as well as other related parameters, then integrated over each of the PLA sections (Ma et al., 2008). Gravitational settling is quite sensitive to the particle size. Large aerosols tend to have high terminal velocity thus fall down back to the surface very quickly.

Wet removal of aerosol by stratiform cloud includes rainout in clouds and washout by rain and snow below clouds. Dust aerosol is generally insoluble but can be mixed with other species such as sulfate, thus a certain fraction of dust particles are hygroscopic and can be activated to form cloud droplets (Sullivan et al., 2009). The in-cloud scavenging rate is proportional to the activated aerosol concentration, cloud fraction, and the sum of autoconversion rate and accretion rate, as well as inversely proportional to the cloud liquid water (Croft et al., 2005). The below-cloud scavenging rate is parame-

ACPD
11, 26477–26520, 2011

terized as a function of precipitation amount (rain and snow respectively) according to Berge (1993).

Deep convection and shallow convective clouds are simulated in CanAM4-PAM as described by Zhang and McFarlane (1995) and von Salzen et al. (2005). Tracers transported by convective clouds are calculated according to von Salzen et al. (2000). The tracer removal rate is determined by upward and downward mass fluxes of air within the convective region, as well as the detrainment rate (Lohmann et al., 1999). For simplicity, wet deposition by convective clouds is not explicitly dependent on size in CanAM4-PAM.

2.3 Parameterization of aerosol radiative properties

Satellite observations provide an overview of the aerosol distribution on a global scale, but hardly distinguish between the different aerosol components. CanAM4-PAM diagnoses the radiative quantities for dust aerosol and for total aerosol, in order to validate model results with the satellite measurements.

Five major aerosol species including sulfate, black carbon (BC), organic carbon (OC), sea salt and mineral dust are considered in CanAM4-PAM. In this study, volcanic, biomass burning, aircraft, ship and other anthropogenic emissions are prescribed for BC and OC aerosols and for the precusor of sulfate aerosol (T. Diehl, personal communication, 2010). Sea salt aerosol is simulated following Ma et al. (2008). Three PLA size sections are used for simulation of internally mixed sulfate, BC and OC aerosols. Sea salt and mineral dust aerosols are assumed externally mixed with two size sections for each.

A size-resolved radiation scheme could be applicable with the PLA method. However, the treatment of aerosol size distribution in the radiation calculation is a potential source of the uncertainty in the estimated aerosol effect (e.g., Tegen and Lacis, 1996; Solomon et al., 2007), which is beyond the scope of this study. Current radiative parameterizations employ simple approximations of the aerosol size distribution. Dust aerosols are assumed in two size modes with mode radii of 0.39 and 1.9 µm, and stan-

ACPD
11, 26477–26520, 2011

dard deviation of 2.0 and 2.15 respectively (Hess et al., 1998). Dust mass loading in two PLA sections are transferred into the two assumed modes for radiation calculation. About 20 % of the mass of dust aerosols are attributed to the accumulation mode, which is consistent with other global model results from AeroCom (Textor et al., 2006).

Dust aerosol is regarded as primarily hydrophobic. Therefore water uptake is not considered in the radiation calculation. The specific extinction coefficient, single scattering albedo and asymmetry factor are functions of dust aerosol size distributions. These radiative parameters are calculated for the two assumed size modes by applying an off-line program based on Mie theory. Radiative properties such as the optical depth of aerosol extinction and absorption are obtained from the provided radiative parameters and aerosol mass at each model layer, and integrated vertically to get the column values.

Relevant parameters for radiation calculation of five aerosol species are summarized in Table 1. Sulfate and sea salt aerosols are simulated following Li et al. (2001) and Dobbie et al. (2003) respectively. BC and OC aerosols are parameterized as in Bäumer et al. (2007) in CanAM4-PAM. Hygroscopic growth of sulfate, sea salt and OC aerosols are limited to the relative humidity (RH) below 95 % in the radiation code, which is similar to other models (Reddy et al., 2005). As in most global climate models, an external mixture is assumed for summing up all aerosol species in calculation of the radiative properties. Aerosol optical depth at a wavelength of 0.55 µm is diagnosed for each of the total aerosol, which will be used to compare with satellite observational data in Sect. 4.

The aerosol direct radiative forcing (ADRF) is determined as the difference in net radiative fluxes at the top of atmosphere (TOA) due to scattering and absorption of radiation by aerosol, which is often investigated to quantify the radiative impact of aerosols on the climate. In CanAM4-PAM, a correlated k-distribution scheme is used for the radiative flux calculation (Li and Barker, 2005). The radiation code is called twice to diagnose the change in net radiative fluxes at TOA that is associated with a change in aerosol concentrations in the model, leaving temperature and other variables constant

ACPD
11, 26477–26520, 2011

(Forster et al., 2007). This approach can be applied for each aerosol component in order to estimate the ADRF of dust aerosol, as well as for the total aerosol.

It has to be pointed out that radiative parameters applied in this study (Hess et al., 1998) possibly overestimate the absorption of mineral dust, which could contribute to the discrepancies in both sign and magnitude of the estimated dust ADRF (Balkanski et al., 2007). A correction of prescribed dust refractive indices according to satellite and ground-based remote sensing data may lead to a more realistic estimation of ADRF (e.g., Kaufman et al., 2001; Moulin et al., 2001). Improvements of dust radiative parameters in the model require more detailed information about the dust aerosol size distribution, mineralogical composition and the mixing state with anthropogenic aerosols, which will be left for the future study.

3 Validation with surface measurements

Two types of model simulations are considered for this study. One is a run driven with climatological sea surface temperatures, while the other uses nudging of model temperature, vorticity and divergence to ERA40 reanalysis data (Merryfield and Scinocca, 2011). As mentioned in Sect. 2.1, dust emissions are very sensitive to changes in model simulated wind speed (U^*). The nudging run applies a relaxation technique so that the analyzed meteorology forces the evolution of dust, in order to minimize the effects of biases in simulated wind fields on dust emissions.

The climate run is performed for five years after a one year spin-up. The nudged run is extended over the time period when observational data is available, with at least two months spin-up. The nudging is applied to both temperature and wind fields and the relaxation time is 6 h.

The threshold wind friction velocity is subject to considerable uncertainty. A tunable parameter is used in CanAM4-PAM to scale the threshold wind friction velocity in order to obtain a global annual mean emission amount within a range of current estimates. This parameter has a weak effect on the spatial and temporal distribution of

ACPD
11, 26477–26520, 2011

dust aerosol (e.g., Timmreck and Schulz, 2004; Cheng et al., 2008). In this study, the tuning parameter for climate run is 0.85 and for nudging run is 0.75.

The probability for the friction velocity to exceed the threshold velocity increases with decreasing value of the scaling parameter, which leads to increasing dust emissions. For given parameter settings, changes in the scaling parameter by ±0.05 lead to changes in dust burden by approximately ∓24 %.

Another important, but uncertain parameter for dust emission is the surface roughness length. As mentioned in Sect. 2.1, dust emission and mass burden decrease with increasing surface roughness. By altering the surface roughness length by ±50 % globally, the annual dust mass burden is changed by around 30 %.

The sensitivity of dust amount to the soil moisture is relatively weak. Dust emission and mass burden vary nonlinearly with the input fraction of soil composition and prescribed soil particle size distributions (Marticorena and Bergametti, 1995; Marticorena et al., 1997).

A climate run of CanAM4-PAM gives global annual emission of dust aerosols as 2700 $\mathrm{Tg\,yr^{-1}}$, while the nudging run yields a dust emission of 2500 $\mathrm{Tg\,yr^{-1}}$ for year 2000. Both are within the range of [1000, 3000] $\mathrm{Tg\,yr^{-1}}$ as estimated by Zender et al. (2004). The climate run gives a column mass burden of dust aerosol of 41.2 $\mathrm{mg\,m^{-2}}$, and the nudging run for year 2000 yields a dust burden of 37.8 $\mathrm{mg\,m^{-2}}$. The latter is in a good agreement with AeroCom estimates from other climate models (range of [8.8, 57.8] with a median of 39.1 $\mathrm{mg\,m^{-2}}$) for the same year (Kinne et al., 2006). Both emission and mass burden of dust are within the estimated range. However, the range of current model estimates is large. This gives evidence for considerable uncertainties in simulations of mineral dust and indicates substantial need for model validation efforts. In this section, various surface measurement datasets are compared with model results. Model results are also validated with satellite retrieved data in Sect. 4.

ACPD
11, 26477–26520, 2011

3.1 Case study in Beijing

One recent case with continuous measurements of aerosol number size distribution is available in the city of Beijing, China, from March 2004 to February 2005. Beijing is located southeast of the main Asian desert areas such as the Gobi and Mongolia. Dust storms prevail in spring and dust aerosols transported from those remote sources dominate in the coarse mode at all time (Seinfeld et al., 2004). Other important aerosol species in this region include sulfate and organic compounds, which are mostly attributed to local sources such as fossil fuel combustion for heating, lateral industry pollution and vehicle emissions in the city area (Wehner et al., 2008).

The sampling site is at Peking University, which is in the northwest of the city. Instruments including two particle counters (TSI3010 and TSI3025) and an APS (Aerodynamic Particle Sizer) were located on a six-floor building, at a height of 20 m above the ground (Wehner et al., 2004). Dry aerosol particles with diameter of 3 nm to 10 μm were collected every ten minutes. Data was post-processed (Wehner et al., 2004) and further averaged to obtain monthly means. Measurements with records in more than 20 days of each month are selected to calculate the monthly averages.

CanAM4-PAM is run with nudging from January 2004 to the end of February 2005. Results from the model simulation are selected at the corresponding times when observations are available. The total aerosol number size distribution at the lowest model layer (at a height of roughly 25 m) is averaged in each month and compared with measurements as shown in Fig. 3. In most of the cases, the observed and simulated size distributions are clearly divided into submicron and supermicron modes as indicated by a dashed line at a radius of 500 nm (e.g., diameter of 1 μm) in Fig. 3. According to Wehner et al. (2008), local traffic and industrial pollutants are responsible for most of the emissions of submicron aerosols. New particle formation is specifically important for nucleation mode aerosols (Yue et al., 2009). Growth of nucleation mode particles through condensation and coagulation of pollutants leads to increases in Aitken and accumulation mode particles. Aside from desert dust transported over long distances,

ACPD
11, 26477–26520, 2011

local construction and road dust contributes to coarse mode particles, too (Wehner et al., 2008; Yue et al., 2009). However, desert dust from non-local sources dominates the concentration of supermicron aerosol.

For all cases shown in Fig. 3, concentration of submicron particles are underestimated by the model. However, highly polluted conditions in urban plumes occur on spatial scales that are not resolved by the model. Therefore, concentrations of submicron particles are underestimated in Fig. 3.

On the other hand, modelled size distributions of supermicron particles agree well with measurements in Fig. 3. For January and February, coarse mode aerosols are underestimated. Since the local wind is strong in Beijing during winter, large particles generated from urban construction and road traffic likely contribute to the observations, which are not included in the global model. Thus differences between model and measurements are more evident in the coarse mode during this season.

In July and August, during the rainy season at Beijing, heavy precipitation leads to efficient wet deposition, which washes out fine to medium size particles and reshapes the number size distribution of aerosols (Yue et al., 2009). Therefore the bi-modal distribution pattern is not as evident as in other months.

In summary, this case comparison in Beijing shows that CanAM4-PAM is able to capture the bi-modal nature of the aerosol size distribution. Model results are consistent with direct measurements of aerosol at the surface, and agree well in the coarse mode where dust particles dominate.

3.2 Surface concentrations in Asia

Dust aerosol mass concentrations near the surface can be estimated from visibility measurements during dust episodes by following an empirical relationship (Shao et al., 2003). Based on regular weather station records, visibility data were collected at 16 stations over Northeast Asia, which covers the Taklamakan Desert, Gobi and some coastal regions influenced by the Asian dust plume. Locations of measurement stations are shown in the top panel of Fig. 4. Data are selected during the main dust season

ACPD
11, 26477–26520, 2011

(spring in Asia), and those taken during the rest of the time period are removed in order to eliminate the impact of other aerosol species. Measurements of surface dust concentrations are averaged over March, April and May of year 2000 and 2001 (Cheng et al., 2008).

CanAM4-PAM is run with nudging for years 2000 and 2001. Simulated dust concentrations at the surface are compared with observations in Fig. 4. The gradients from the source regions to the distant ocean are well captured by the model. Note that global model estimates of dust aerosol are generally uncertain and perform rather poorly in Asia (e.g., Kinne et al., 2006), so that it is meaningful to validate the CanAM4-PAM especially for this region. Figure 5 shows a comparison between measured and simulated surface dust concentration in Asia during boreal spring. The average ratio of model results to measurements is 0.92.

3.3 Surface concentrations at marine sites

Long-term measurements of surface dust mass concentrations are available from the University of Miami (Prospero, 1999). Data were collected at 21 remote marine sites and cover a time period of about 10 yr in total. The dust mass concentration is derived from observed aluminum concentrations by assuming a certain percent of aluminum content in mineral dust aerosols (Prospero, 1999). Measured data are averaged over multiple years to obtain an annual mean and 12 monthly means, and compared with model simulations.

For this comparison, CanAM4-PAM is run with climatological sea surface temperatures for 5 yr. Simulated dust aerosol concentrations are taken from the grid points corresponding to the location of the observations. A 5-yr averaged annual mean of simulated dust mass concentration is compared with the measurements in Fig. 6. The ratio between simulated and measured data is 1.28. When dust concentration is high, that is, near source regions, model results align well with the 1:1 line, although the concentrations are slightly underestimated. A likely reason for the underestimation is local dust sources that are not resolved by the GCM.

ACPD
11, 26477–26520, 2011

When dust concentration is low, that is, far from source regions, the model tends to overestimate the concentrations. This may be explained by insufficient deposition near source regions, which leads to an excessive transport of more aerosols to remote areas. There is some support for this hypothesis from results for deposition fluxes in Sect. 3.4.

A comparison of monthly mean dust surface concentrations is shown in Fig. 7. The model estimates agree well with the observations near the source regions in most cases. The seasonality is similar too. For example, for two Asian sites near Japan, CHEJU and HEDO OKINAWA, observed and simulated peaks are in spring when Asian dust prevails. Two Pacific sites, MIDWAY ISLAND and OAHU HAWAII, are farther from the continent and less influenced by the Asian plume. Although peaks remain in spring here, concentrations are much lower than at the two Asian sites. Model results are higher than observations at these two Pacific sites. It is consistent with the overestimation in Fig. 6, when dust concentration is low.

The two sites, BERMUDA and RSMAS MIAMI in Central America are potentially affected by the Saharan dust plume. Model results show good timing of dust peaks in summer, when Saharan dust is particularly important. For more remote sites such as sites in the South Pacific or in Antarctica, the model predicts much larger dust surface concentrations than the measurement, which is consistent with results in Fig. 6.

3.4 DIRTMAP data

The Dust Indicators and Records of Terrestrial and MArine Palaeoenvironments (DIRTMAP) database provides a global dataset for the dust deposition rate, which is based on records from ice cores, marine sediments and terrestrial (loess) deposits (Kohfeld and Harrison, 2001). Data of version 2.0 are used for this study.

DIRTMAP data have been post-processed by removing short-term signals and possibly contaminated sites (Kohfeld and Harrison, 2001). Ice core records are mainly located in polar regions such as Greenland and Antarctica. The remaining ice core records are taken from mountains of South America and the Tibetan Plateau, where

ACPD
11, 26477–26520, 2011

local environment may have potential impacts on aerosol sources. Marine sediment data are mostly measured at open-ocean sites by excluding records contaminated with fluvial input, ice-rafted detritus and lateral sediment redistribution (Mahowald et al., 1999). Terrestrial deposits are obtained in North America, Central Europe as well as the Chinese Loess Plateau. Continental records are susceptible to local disturbances, e.g., biogenic residues, agriculture, constructions and road traffic (Kohfeld and Harrison, 2001; Tegen et al., 2002). Therefore no terrestrial deposit data are used for comparison in this study. Both ice core and marine sediment records are long-term integrated yet have been used as dust indicators under modern conditions (Mahowald et al., 1999), in particular for equilibrium climate (Tegen et al., 2002).

Dust deposition rates obtained from ice core and marine sediment records from the DIRTMAP 2.0 dataset are shown in the upper panel of Fig. 8. Model results in Fig. 8 for the total rate of dry and wet deposition are diagnosed from the CanAM4-PAM simulation for climatological conditions.

In the upper panel of Fig. 8, peak values are near the dust source regions such as Western Sahara, Middle East and East Asia. The location and magnitude of the dust deposition maxima are well captured by the model, which indicates a realistic representation of dust plumes from major source regions in the model, in particular near West Africa and over the Atlantic Ocean. However, simulated deposition rates are lower in the Arabian Sea and Northwest Pacific. These regions are influenced by sources in Middle East and East Asia respectively. Owing to the fact that giant particles are ignored in the dust emission scheme (see Sect. 2.1) and the prescribed Asian soil types are mostly attributed to the small size mode (Cheng et al., 2008), the model is expected to have a lower rate of dry deposition in this region. The less effective dry deposition allows more dust to be transported to remote areas. It is likely partly responsible for the model overestimation of dust surface concentration far from sources (Fig. 6 and Sect. 3.3), too.

In the Southern Hemisphere, a reduction in deposition rate with distance from sources in Australia is captured by the model. Simulated deposition rates are underestimated

ACPD
11, 26477–26520, 2011

in the Indian Ocean and South Atlantic Ocean. There is also evidence of low aerosol AOD in these regions (see Sect. 4.1), which possibly lead to insufficient wet deposition of dust by mixing with sulfate or organic aerosols.

In summary, model results for surface measurements of size distributions, mass concentrations, and deposition are in good agreement with observations near dust sources. Dust plume extension and seasonal distribution are also realistic. Most discrepancies between model simulation and observations occur in remote areas far from the dust sources, where the model tends to overestimate aerosol amounts and deposition.

4 Validation with satellite measurements

Satellite data have been widely used to study aerosol effects on the large scale (Kaufman et al., 2002) and for validation of GCM simulations (e.g., Kinne et al., 2006). In this section model results are compared with retrieved data from passive instruments onboard satellites, in particular for aerosol optical depth (AOD) at 0.55 µm wavelength and aerosol direct radiative forcing (ADRF).

4.1 Aerosol Optical Depth (AOD)

Note that satellite observations have difficulty distinguishing between different aerosol species, thus this section focuses on the total AOD instead of the dust AOD. Three datasets of retrieved AOD from satellites are applied for comparisons with model results. The first is based on measurements from the MODerate Resolution Imaging Spectroradiometer (MODIS), which is onboard NASA's Terra platform (Remer et al., 2005). For this study, archived data from the MOD08_M3 collection 5 dataset is used. Over highly reflective surfaces such as deserts, AOD retrievals from this dataset are not very reliable owing to the assumption of a Lambertian surface (Abdou et al., 2005). More accurate retrievals over land are available from measurements with the Multiangle

ACPD
11, 26477–26520, 2011

Imaging SpectroRadiometer (MISR) on board Terra. The instrument is able to provide reliable retrievals both over land and ocean. The MISR AOD product version 3.1 is used for this study (Kahn et al., 2005). Both MODIS and MISR data are available online through the NASA Giovanni interface (http://disc.sci.gsfc.nasa.gov/giovanni/).

As a third dataset, a combined MODIS/MISR dataset from van Donkelaar et al. (2006, 2010) was also considered for this study. For this dataset, the retrieved albedo from MODIS is used to divide the Earth's surface into different domains. Monthly averaged MODIS and MISR AOD are then compared against ground-based measurements of AOD from AERONET within each domain. Outliers of AOD values are filtered out. Both MODIS and MISR AOD with fine mode fraction smaller than 20 % are also filtered out to reduce the influence of large particles on the retrieval. AOD after albedo-filtering and fine-mode-filtering are provided as a combined dataset (between 60° S and 75° N) from year 2001 to 2006 with a resolution of 0.1°×0.1°. Data near the poles are set to be zero (van Donkelaar et al., 2010).

For comparisons with satellite retrievals, the model is run with nudging for years 2001 to 2006. The model captures the main aerosol plumes over West Africa, Middle East and East Asia (Fig. 9). Most of the sources are in the Northern Hemisphere. Main deserts in Asia, such as the Taklamakan and Gobi, are well represented by the model. High AODs in east Asia and India are mostly caused by sulfate and BC aerosols from human activity. Model results are consistent with satellite estimates for the Asian plume over the North Pacific, but fail to reproduce the southward extension around Indonesia. Aside from major desert regions, secondary dust sources are captured by the model as well. For example, deserts in Chile and Peru, and deserts in Australia.

The global mean AOD (60° S to 75° N) of the total aerosol is 0.138 from the simulation. The corresponding MODIS and MISR AOD are 0.108 and 0.112 respectively, excluding points with missing data. The AOD of the combined dataset is 0.129, which is close to the model result.

Figure 10 shows the seasonal variation of the model results in comparison with satellite measurements of AOD. In winter, West Africa is the main source of dust on the

ACPD
11, 26477–26520, 2011

globe. Spring is the most dusty season, especially in Asia. The Asian plume is largely extended and reaches to the west coast of Canada and the US. High AOD values occur for West Africa and the Middle East in summer, which is well represented by the simulation results. The highest AOD values occur during spring and summer and are located over Asia, which is attributed to sulfate and carbonaceous aerosols. In boreal autumn, South America and Australia are highlighted as secondary dust sources. However, CanAM4-PAM fails to reproduce the large AOD in South Africa and South America during boreal summer and autumn, that is, winter and spring in the Southern Hemisphere. High AOD values during this period are mainly caused by vegetation fires. This may indicate a lack of emissions from biomass burning in these regions.

The dust AOD and total AOD are also calculated for a run nudged for year 2000, in order to compare with AeroCom estimates from other GCMs. CanAM4-PAM produces a dust AOD and total AOD of 0.042 and 0.126 respectively, while the AeroCom median values are 0.032 for dust and 0.127 for total aerosol (Kinne et al., 2006).

4.2 Aerosol Direct Radiative Forcing (ADRF)

MODIS measures the clear-sky SW radiances, which can be converted to TOA SW fluxes with empirical Angular Distribution Models (ADMs) developed from CERES (Clouds and the Earth's Radiant Energy System) following the procedure in Loeb et al. (2005). The TOA ADRF is then derived from the SW fluxes by using the approach of Loeb and Smith (2005). The MODIS/CERES ADRF product is for total aerosol only. For contributions of individual types of aerosols to the total ADRF, Zhao et al. (2010) calculates the AOD ratio of sulfate, sea salt, dust, BC and OC to the total aerosol AOD according to simulation results from the Goddard Global Ozone Chemistry Aerosol Radiation and Transport (GOCART) model. Both total ADRF and component ADRF are available with a resolution of $1^\circ \times 1^\circ$ for year 2001 (Zhao et al., 2010).

Simulated ADRF at TOA for the year 2001 for clear-sky conditions are compared to MODIS/CERES ADRF as well as the derived dust ADRF in Fig. 11. Satellite data are not reliable in polar regions and are therefore ignored. ADRF over continents is

ACPD
11, 26477–26520, 2011

also masked out because the land surface albedo influences the ADRF. The current GCM estimate and satellite retrieval of ADRF show a variety of dependences on the land surface albedo assumptions, especially in desert and snow covered regions (e.g., Schulz et al., 2006; Yu et al., 2006). Thus ADRF is only plotted over ocean in Fig. 11 to investigate into the effect of aerosols (e.g., Myhre et al., 2008).

Figure 11 shows a good agreement for the dust forcing. Both magnitude and position of dust plumes off West Africa and Middle East are consistent with the satellite data. The extension of Asian dust plume to the North Pacific is underestimated to some degree. The total ADRF from CanAM4-PAM simulation is less negative around 10° S to 10° N off the west coast of Africa, which is likely due to the missing OC sources from biomass burning, as indicated in Sect. 4.1. A relatively weak forcing of Asian aerosol over the North Pacific is partly attributed to the underestimation of BC and sulfate aerosols. The less negative forcing over the ocean in the Southern Hemisphere could be due to sea salt (figures of non-dust aerosols are not shown).

In general, the simulated ADRF of dust and total aerosols over ocean exhibit consistent global patterns with the satellite measurements. The total and dust ADRF from CanAM4-PAM are -4.76 and $-1.24\,\mathrm{W\,m^{-2}}$ respectively. The MODIS/CERES ADRF and derived dust ADRF are -6.53 and $-1.20\,\mathrm{W\,m^{-2}}$. Discrepancies between the simulated and retrieved total ADRF are mainly related to non-dust aerosols.

5 Conclusions

A size-resolved numerical scheme in an experimental version of the fourth generation Canadian Atmospheric Global Climate Model (CanAM4-PAM) is applied to simulations of the global dust cycle. In the model, emission, transport as well as deposition of dust aerosols are parameterized in terms of the size distribution of particles. The simulated global mean emission amount and mass burden of dust aerosols are within the range of estimates from other GCMs. CanAM4-PAM shows a rather good agreement with observations for size distributions, mass concentrations and deposition rates from

ACPD
11, 26477–26520, 2011

multiple surface-based datasets. Discrepancies between the model and observations are mostly within the range of uncertainty of observations. Consistent biases relative to different datasets are possibly attributed to underestimates for deposition rates in the model, indicating the need for improvements of parameterizations for unresolved processes.

In the current study, the model performs well in reproducing major dust sources such as West Africa, Middle East as well as East Asia. However, secondary sources, especially sources in the Southern Hemisphere are not very well represented. Compared to large desert regions in the Northern Hemisphere, deserts in South America, South Africa and Australia are rather sparse. Emission and distribution of dust in the Southern Hemisphere are affected by continental topography and local meteorological conditions, which are not well resolved in a GCM. It is noted that dust comparisons with both short-term (Sects. 3.1 and 3.2) and long-term (Sect. 3.3) surface measurements show good consistencies, which is a significant improvement from previous dust models (Huneeus et al., 2011) and mainly attributed to the size-resolved scheme applied in this simulation.

For dust and other major aerosols, both AOD and ADRF results are compared with satellite retrieval and show good consistency. In this study, the size distribution of dust aerosol is traced through the microphysics scheme in CanAM4-PAM. However, only the mass mixing ratio from the PLA scheme is transferred to the radiation scheme. In a future study, aerosol radiative calculation will be improved in CanAM4-PAM. PLA size parameters in addition to the mass mixing ratio will be used together for radiation calculations, which may help to simulate the radiative properties more accurately.

Giant particles of erodible dust aerosol are ignored in this study, which has little impact on estimates of global mass burden and radiative forcing of dust. Another simplification is the mixing of dust with soluble aerosols. The model accounts for the slight solubility of dust in stratiform clouds, which is expected to lead to underestimates in wet deposition rates and results in a higher dust surface concentration, particularly in the tropical regions enriched with sulfate and organic aerosols.

ACPD
11, 26477–26520, 2011

There is no direct measurement of aerosol size distribution on a global scale. As most GCMs are expected to soon include schemes for size-resolved simulation of aerosols, an integrated dataset with global aerosol size information is needed. Moreover, both AOD and ADRF datasets from satellite retrieval are 2-dimensional. The Cloud-Aerosol Lidar and Infrared Pathfinder Satellite Observation (CALIPSO) will provide layered data of aerosol properties. The new dataset will help to understand and simulate dust aerosol more realistically in GCMs.

Acknowledgements. This study is part of the CAFC (Cloud-Aerosol Feedbacks and Climate) network, which is funded by CFCAS (Canadian Foundation for Climate and Atmospheric Science). We thank Ina Tegen and Birgit Wehner for providing the dust emission input files and observational data in Beijing respectively. Thomas Diehl from NASA is acknowledged for his help with the emission files of sulfate, BC and OC aerosols. We also thank for Joseph Prospero for providing the global measurement data of dust surface concentrations. X.-P. Zhao and Norman Loeb are acknowledged for their help with the ADRF satellite data.

References

Abdou, W. A., Diner, D. J., Martonchik, J. V., Bruegge, C. J., Kahn, R. A., Gaitley, B. J., and et al: Comparison of coincident multiangle imaging spectroradiometer and moderate resolution imaging spectroradiometer aerosol optical depth over land and ocean scenes containing aerosol robotic network sites, J. Geophys. Res., 110, D10S07, doi:10.1029/2004JD004693, 2005. 26496

Arimoto, R., Ray, B. J., Lewis, N. F., and Tomza, U.: Mass-particle size distribution of atmospheric dust and the dry deposition of dust to the remote ocean, J. Geophys. Res., 102, 15867–15874, 1997. 26485

Arora, V. and Boer, G.: A parameterization of leaf phenology for the terrestrial ecosystem component of climate models, Global Change Biol., 11, 39–59, 2005. 26482

Balkanski, Y., Shculz, M., Claquin, T., and Guibert, S.: Reevaluation of mineral dust aerosol radiative forcings suggests a better agreement with satellite and AERONET data, Atmos. Chem. Phys., 7, 81–95, doi:10.5194/acp-7-81-2007, 2007. 26489

ACPD

11, 26477–26520, 2011

Bäumer, D., Lohmann, U., Lesins, G., Li, J., and Croft, B.: Parameterizing the optical properties of carbonaceous aerosols in the Canadian Centre for Climate Modeling and Analysis Atmospheric General Circulation Model with impacts on global radiation and energy fluxes, J. Geophys. Res., 112, D10207, doi:10.1029/2006JD007319, 2007. 26488

Berge, E.: Coupling of wet scavenging of sulphur to clouds in a numerical weather prediction model, Tellus, 45B, 1–22, 1993. 26487

Boer, G. J.: A hybrid moisture variable suitable for spectral GCMs, in: Research Activity in Atmospheric and Oceanic Modelling, Report No. 21, WMO/TD 665, Geneva, Switzerland, 1995. 26485

Cheng, T., Peng, Y., Feichter, J., and Tegen, I.: An improvement on the dust emission scheme in the global aerosol-climate model ECHAM5-HAM, Atmos. Chem. Phys., 8, 1105–1117, doi:10.5194/acp-8-1105-2008, 2008. 26483, 26484, 26490, 26493, 26495

Croft, B., Lohmann, U., and von Salzen, K.: Black carbon aging in the Canadian Centre for Climate Modelling and Analysis General Circulation Model, Atmos. Chem. Phys, 5, 1383–1419, doi:10.5194/acp-5-1383-2005, 2005. 26486

Dobbie, S., Li, J., Harvey, R., and Chýlek, P.: Sea-salt optical properties and GCM forcing at solar wavelengths, Atmos. Res., 65, 211–233, 2003. 26488

Dubovik, O., Sinyuk, A., Lapyonok, T., Holben, B. N., Mishchenko, M., Yang, P., Eck, T. F., Volten, H., Munoz, O., Veihelmann, B., van der Zande, W. J., Leon, J.-F., Sorokin, M., and Slutsker, I.: Application of spheroid models to account for aerosol particle nonsphericity in remote sensing of desert dust, J. Geophys. Res., 111, D11208, doi:10.1029/2005JD006619, 2006. 26480

Fécan, F., Marticorena, B., and Bergametti, G.: Parametrization of the increase of the aeolian erosion threshold wind friction velocity due to soil moisture for arid and semi-arid areas, Ann. Geophys., 17, 149–157, doi:10.1007/s00585-999-0149-7, 1999. 26483

Forster, P., Ramaswamy, V., Artaxo, P., Berntsen, T., Betts, R., Fahey, D., Haywood, J., Lean, J., Lowe, D., Myhre, G., Nganga, J., Prinn, R., Raga, G., Schultz, M., and Van Dorland, R.: Changes in atmospheric constituents and in radiative forcing, in: Climate change 2007: The physical science basis., in: Contribution of Working Group I to the Fourth Assessment Report of the Intergovernmental Panel on Climate, edited by Solomon, S., Qin, D., Manning, M., Chen, Z., Marquis, M., Averyt, K. B., Tignor, M., and Miller, H. L., Cambridge University Press, Cambridge, United Kingdom and New York, NY, USA, 2007. 26489

Gong, S. L., Barrie, L. A., Blanchet, J.-P., von Salzen, K., Lohmann, U., Lesins, G.,

ACPD
11, 26477–26520, 2011

and et al: CAM: A size-segregated simulation of atmospheric aerosol processes for climate and air quality models. 1. Module Development, J. Geophys. Res., 108, 4007, doi:10.1029/2001JD002002, 2003. 26479, 26484

Hess, M., Koepke, P., and Schult, I.: Optical properties of aerosols and clouds: The software package OPAC, B. Am. Meteorol. Soc., 79, 831–844, 1998. 26488, 26489

Huneeus, N., Schulz, M., Balkanski, Y., Griesfeller, J., Prospero, J., and et al.: Global dust model intercomparison in AeroCom phase I, Atmos. Chem. Phys., 11, 7781–7816, doi:10.5194/acp-11-7781-2011, 2011. 26479, 26500

Jickells, T. D., An, Z. S., Andersen, K. K., Baker, A. R., Bergametti, G., Brooks, N., Cao, J. J., Boyd, P. W., Duce, R. A., Hunter, K. A., Kawahata, H., Kubilay, N., laRoche, J., Liss, P. S., Mahowald, N., Prospero, J. M., Ridgwe, A. J., Tegen, I., and Torres, R.: Global iron connections between desert dust, ocean biogeochemistry and climate, Science, 308, 67–71, 2005. 26479

Kahn, R. A., Gaitley, B. J., Martonchik, J. V., Diner, D. J., Crean, K. A., and Holben, B.: Multiangle Imaging SpectroRadiometer (MISR) global aerosol optical depth validation based on 2 years of coincident Aerosol Robotic Network (AERONET) observations, J. Geophys. Res., 110, D10S04, doi:10.1029/2004JD004706, 2005.

Kaufman, Y. J., Tanré, D., Dubovik, O., Karnieli, A., and Remer, L. A.: Absorption of sunlight by dust as inferred from satellite and ground-based remote sensing, Geophys. Res. Lett., 28, 1479–1482, 2001. 26480, 26497

Kaufman, Y. J., Tanré, D., and Boucher, O.: A satellite view of aerosols in the climate system, Nature, 419, 215–223, 2002. 26489

Kaufman, Y. J., Koren, I., Remer, L. A., Tanré, D., Ginoux, P., and Fan, S.: Dust transport and deposition observed from the Terra-Moderate Resolution Imaging Spectroradiometer (MODIS) spacecraft over the Atkantic Ocean, J. Geophys. Res., 110, D10S12, doi:10.1029/2003JD004436, 2005. 26496

Kinne, S., Schulz, M., Textor, C., Guibert, S., Balkanski, Y., Bauer, S. E., Berntsen, T., Berglen, T. F., Boucher, O., Chin, M., Collins, W., Dentener, F., Diehl, T., Easter, R., Feichter, J., Fillmore, D., Ghan, S., Ginoux, P., Gong, S., Grini, A., Hendricks, J., Herzog, M., Horowitz, L., Isaksen, I., Iversen, T., Kirkevag, A., Kloster, S., Koch, D., Kristjansson, J. E., Krol, M., Lauer, A., Lamarque, J. F., Lesins, G., Liu, X., Lohmann, U., Montanaro, V., Myhre, G., Penner, J. E., Pitari, G., Reddy, S., Seland, O., Stier, P., Takemura, T., and Tie, X.: An AeroCom initial assessment – optical properties in aerosol component modules of global

ACPD
11, 26477–26520, 2011

models, Atmos. Chem. Phys., 6, 1815–1834, doi:10.5194/acp-6-1815-2006, 2006. 26480
Kohfeld, K. and Harrison, S. P.: DIRTMAP: The geologic record of dust, Earth Sci., 54, 81–114, 2001. 26478, 26479, 26490, 26493, 26496, 26498
Li, J. and Barker, H. W.: A radiation algorithm with correlated k-distribution. Part I: local thermal equilibrium, J. Atmos. Sci., 62, 286–309, 2005. 26480, 26494, 26495, 26517
Li, J., Wong, J. G. D., Dobbie, J. S., and Chýlek, P.: Parameterization of the optical properties of sulfate aerosols, J. Atmos. Sci., 58, 193–209, 2001. 26488
Loeb, N. G. and Smith, N. M.: Top-of-atmosphere direct radiative effect of aerosols over global oceans from merged CERES and MODIS observations, J. Clim., 18, 3506–3526, 2005. 26488
Loeb, N. G., Kato, S., Loukachine, K., and Smith, N. M.: Angular distribution models for top-of-atmosphere radiative flux estimation from the Clouds and the Earth's Radiant Energy System instrument on the Terra satellite. Part 1: Methodology, J. Ocean and Atmos. Tech., 22, 338–351, 2005. 26498
Lohmann, U., Von Salzen, K., McFarlane, N., Leighton, H. G., and Feichter, J.: The tropospheric sulfur cycle in the Canadian general circulation model, J. Geophys. Res., 104, 26833–26858, 1999. 26498
Ma, X., von Salzen, K., and Li, J.: Modelling sea salt aerosol and its direct and indirect effects on climate, Atmos. Chem. Phys., 8, 1311–1327, doi:10.5194/acp-8-1311-2008, 2008. 26487
Mahowald, N., Kohfeld, K., Hansson, M., Balkanski, Y., Harrison, S. P., Prentice, I. C., Schulz, M., and Rodhe, H.: Dust sources and deposition during the last glacial maximum and current climate: A comparison of model results with paleodata from ice cores and marine sediments, J. Geophys. Res., 104, 15895–15916, 1999. 26486, 26487
Marticorena, B. and Bergametti, G.: Modeling the atmospheric dust cycle: 1. Design of a soil-derived dust emission scheme, J. Geophys. Res., 100, 16415–16430, 1995. 26495
Marticorena, B., Bergametti, G., B., A., Callot, Y., NDoume, C., and Legrand, M.: Modeling the atmospheric dust cycle: 2. Simulation of Saharan dust sources, J. Geophys. Res., 102, 4387–4404, 1997. 26482, 26483, 26484, 26490
Merryfield, W. J. and Scinocca, J.: The Second Coupled Historical Forecasting Project (CHFP2): I. Models and Initialization, Mon. Weather Rev., submitted, 2011. 26482, 26490
Merryfield, W. J., McFarlane, N., and Lazare, M.: A generalized hybrid transformation for tracer advection, in: Research Activity in Atmospheric and Oceanic Modelling, CAS/JSC WGNE Blue Book, Report No. 33, 13–14, WMO/TD 1161, Geneva, Switzerland, 2003. 26489

ACPD
11, 26477–26520, 2011

Min, Q.-L., Li, R., Lin, B., Joseph, E., Wang, S., Hu, Y., Morris, V., and Chang, F.: Evidence of mineral dust altering cloud microphysics and precipitation, Atmos. Chem. Phys., 9, 3223–3231, doi:10.5194/acp-9-3223-2009, 2009. 26485

Moulin, C., Howard, R. G., Banzon, V. F., and Evans, R. H.: Assessment of Saharan dust absorption in the visible from SeaWiFS imagery, J. Geophys. Res., 106, 18239–18249, 2001. 26479

Myhre, G., Berglen, T. F., Johnsrud, M., Hoyle, C. R., Berntsen, T. K., Christopher, S. A., Fahey, D. W., Isaksen, I. S. A., Jones, T. A., Kahn, R. A., Loeb, N., Quinn, P., Remer, L., Schwarz, J. P., and Yttri, K. E.: Modelled radiative forcing of the direct aerosol effect with multi-observation evaluation, Atmos. Chem. Phys., 9, 1365–1392, doi:10.5194/acp-9-1365-2009, 2009. 26489

Prigent, C., Tegen, I., Aires, F., Marticorena, B., and Zribi, M.: Estimation of the aerodynamic roughness length in arid and semi-arid regions over the globe with the ERS scatterometer, J. Geophys. Res., 110, D09205, doi:10.1029/2004JD005370, 2005. 26499

Prospero, J. M.: Particle flux in the ocean, in: The atmospheric transport of particles to the ocean, edited by: Ittekott, V., Schäfer, P., Honjo, S., and Depetris, P., John Wiley & Sons, Chichester, UK, 19–52, 1996. 26483

Prospero, J. M.: Long-term measurements of the transport of African mineral dust to the southeastern United States: Implications for regional air quality, J. Geophys. Res., 104, 15917–15927, 1999. 26480

Reader, M. C., Fung, I., and McFarlane, N.: The Mineral dust aerosol cycle during the last glacial maximum, J. Geophys. Res., 104, 9381–9398, 1999. 26493, 26515, 26516

Reddy, M. S., Boucher, O., Bellouin, N., Schulz, M., Balkanski, Y., Dufresne, J.-L., and Pham, M.: Estimates of global multicomponent aerosol optical depth and direct radiative perturbation in the Laboratoire de Meteorologie Dynamique general circulation model, J. Geophys. Res., 110, D10S16, doi:10.1029/2004JD004757, 2005. 26479

Remer, L. A., Kaufman, Y. J., Mattoo, S., and et al: The MODIS algorithm, products and validation, J. Atmos. Sci., 62, 947–973, 2005. 26488

Rosenfeld, D., Rudich, Y., and Lahav, R.: Desert dust suppressing precipitation: A possible desertification feedback loop, Proc. Natl. Acad. Sci., 98, 5975–5980, 2001. 26496

Sassen, K.: Indirect climate forcing over the western US from Asian dust storms, Geophys. Res. Lett., 29, 1465, doi:10.1029/2001GL014051, 2002. 26479
26479

ACPD
11, 26477–26520, 2011

Schulz, M., Textor, C., Kinne, S., Balkanski, Y., Bauer, S., Berntsen, T., Berglen, T., Boucher, O., Dentener, F., Guibert, S., Isaksen, I. S. A., Iversen, T., Koch, D., Kirkeväg, A., Liu, X., Montanaro, V., Myhre, G., Penner, J. E., Pitari, G., Reddy, S., Seland, O., Stier, P., and Takemura, T.: Radiative forcing by aerosols as derived from the AeroCom present-day and preindustrial simulations, Atmos. Chem. Phys., 6, 5225–5246, doi:10.5194/acp-6-5225-2006, 2006. 26478, 26499

Seinfeld, J. H., Carmichael, G. R., Arimoto, R., Conant, W. C., Brechtel, F. J., Bates, T. S., Cahill, T. A., Clarke, A. D., Doherty, S. J., Flatau, P. J., Huebert, B. J., Kim, J., Markowicz, K. M., Quinn, P. K., Russell, L. M., Russell, P. B., Shimizu, A., Shinozuka, Y., Song, C. H., Tang, Y., Uno, I., Vogelmann, A. M., Weber, R. J., Woo, J.-H., and Zhang, X. Y.: ACE-ASIA: Regional Climatic and Atmospheric Chemical Effects of Asian Dust and Pollution, B. Am. Meteorol. Soc., 85, 367–380, 2004. 26491

Shao, Y., Yang, Y., Wang, J., and et al: Northeast Asian dust storms: Real-time numerical predictions and validation, J. Geophys. Res., 108, 4691, doi:10.1029/2003JD003667, 2003. 26492

Solomon, S., Qin, D., Manning, M., Chen, Z., Marquis, M., Averyt, K., Tignor, M., and Miller, H. E.: Climate Change 2007: The Physical Basis. Contribution of Working Group I to the Fourth Assessment Report of the Intergovernmental Panel on Climate Change, Cambridge Univ. Press, Cambridge, UK and New York, USA, 996 pp., 2007. 26478, 26479, 26487

Stier, P., Feichter, J., Kinne, S., Kloster, S., Vignati, E., Wilson, J., Ganzeveld, L., Tegen, I., Werner, M., Balkanski, Y., Schulz, M., Boucher, O., Minikin, A., and Petzold, A.: The aerosol-climate model ECHAM5-HAM, Atmos. Chem. Phys., 5, 1125–1156, doi:10.5194/acp-5-1125-2005, 2005. 26479, 26484

Sullivan, R. C., Moore, M. J. K., Petters, M. D., Kreidenweis, S. M., Roberts, G. C., and Prather, K. A.: Effect of chemical mixing state on the hygroscopicity and cloud nucleation properties of calcium mineral dust particles, Atmos. Chem. Phys., 9, 3303–3316, doi:10.5194/acp-9-3303-2009, 2009. 26486

Tegen, I. and Fung, I.: Modeling of mineral dust in the atmosphere: Sources, transport, and optical thickness, J. Geophys. Res., 99D, 22897–22914, 1994. 26479

Tegen, I. and Lacis, A. A.: Modeling of particle size distribution and its influence on the radiative properties of mineral dust aerosol, J. Geophys. Res., 101, 19237–19244, 1996. 26487

Tegen, I., Harrison, S. P., Kohfeld, K., and Prentice, I. C.: Impact of vegetation and preferential source areas on global dust aerosol: Results from a model study, J. Geophys. Res., 107,

ACPD
11, 26477–26520, 2011

4576, doi:10.1029/2001JD000963, 2002. 26482, 26484, 26495
Textor, C., Schulz, M., Guibert, S., Kinne, S., and et al: Analysis and quantification of the diversities of aerosol life cycles within AeroCom, Atmos. Chem. Phys., 6, 1777–1813, doi:10.5194/acp-6-1777-2006, 2006. 26478, 26479, 26486, 26488
Timmreck, C. and Schulz, M.: Significant dust simulation differences in nudged and climatological operation mode of the AGCM ECHAM, J. Geophys. Res., 109, D13202, doi:10.1029/2003JD004381, 2004. 26490
van Donkelaar, A., Martin, R. V., and Park, R. J.: Estimating ground-level PM2.5 using aerosol optical depth determined from satellite remote sensing, J. Geophys. Res., 111, D21201, doi:10.1029/2005JD006996, 2006. 26497
van Donkelaar, A., Martin, R. V., Brauer, M., Kahn, R., Levy, R., Verduzco, C., and Villeneuve, P. J.: Global estimates of ambient fine particulate matter concentrations from satellite-based aerosol optical depth: Development and application, Environ. Health Perspec., 118, 847–855, doi:10.1289/ehp.0901623, 2010. 26497
Verseghy, D. L.: CLASS: A Canadian Land Surface Scheme for GCMs. I. Soil model, International Journal of Climatology, 11, 111–133, 1991. 26484
von Salzen, K.: Piecewise log-normal approximation of size distributions for aerosol modelling, Atmos. Chem. Phys., 6, 1351–1372, doi:10.5194/acp-6-1351-2006, 2006. 26480, 26481, 26482
von Salzen, K., Leighton, H. G., Ariya, P. A., Barrie, L. A., Gong, S. L., Blanchet, J. P., Spacek, L., Lohmann, U., and Kleinman, L. I.: The sensitivity of sulphate aerosol size distributions and CCN concentrations over North America to SO_x emissions and H_2O_2 concentrations, J. Geophys. Res., 105, 9741–9766, 2000. 26487
von Salzen, K., McFarlane, N. A., and Lazare, M.: The role of shallow low convection in the water and energy cycles of the atmosphere, Clim. Dynam., 25, 671–699, 2005. 26481, 26487
Wang, A., Price, D. T., and Arora, V.: Estimating changes in global vegetation cover (1850-2100) for use in climate models, Global Biogeochem. Cy., 20, GB3028, doi:10.1029/2005GB002514, 2006. 26483
Wehner, B., Wiedensohler, A., Tuch, T. M., Wu, Z. J., Hu, M., Slanina, J., and Kiang, C. S.: Variability of the aerosol number size distribution in Beijing, China: new particle formation, dust storms, and high continental background, Geophys. Res. Lett., 31, L22108, doi:10.1029/2004GL021596, 2004. 26491

ACPD
11, 26477–26520, 2011

Wehner, B., Birmili, W., Ditas, F., Wu, Z., Hu, M., Liu, X., Mao, J., Sugimoto, N., and Wiedensohler, A.: Relationships between submicronmeter particulate air pollution and air mass history in Beijing, China, 2004-2006, Atmos Chem. Phys., 8, 6155–6168, doi:10.5194/acp-8-6155-2008, 2008. 26491, 26492

Yu, H., Kaufman, Y. J., Chin, M., and et al.: A review of measurement-based assessments of the aerosol direct radiative effect and forcing, Atmos. Che. Phys., 6, 613–666, doi:10.5194/acp-6-613-2006, 2006. 26499

Yue, D., Hu, M., Wu, Z., Wang, Z., Guo, S., Wehner, B., Nowak, A., Achtert, P., Wiedensohler, A., Jung, J., Young, K. J., and Liu, S.: Characteristics of aerosol size distributions and new particle formation in the summer in Beijing, J. Geophys. Res., 114, D00G12, doi:10.1029/2008JD010894, 2009. 26491, 26492

Zender, C. S., Miller, R. L., and Tegen, I.: Quantifying Mineral Dust Mass Budgets: Terminology, Constraints, and Current Estimates, Eos Trans. AGU, 85, 509, doi:10.1029/2004EO480002, 2004. 26479, 26490

Zhang, G. J. and McFarlane, N. A.: Sensitivity of Climate Simulations to the Parameterization of Cumulus Convection in the Canadian Climate Centre General Circulation Model, Atmos. Ocean, 33, 407–446, 1995. 26487

Zhang, L.-M., Gong, S.-L., Padro, J., and Barrie, L.: A size-segregated particle dry deposition scheme for an atmospheric aerosol module, Atmos. Environ., 35, 549–560, 2001. 26486

Zhao, X.-P., Loeb, N. G., Laszlo, I., and Zhou, M.: Global component aerosol direct radiative effect at the top of atmosphere, Int. J. Remote Sens., 32, 633–655, 2010. 26498

Zobler, L.: A world soil file for global climate modeling, Tech. Rep. 87802, Tech. Rep. NASA, 1986. 26484

ACPD
11, 26477–26520, 2011

Table 1. Prescribed parameters of five major aerosols for radiation calculations in CanAM4-PAM.

	Sulfate	BC	OC	Sea salt	Dust
r_{mode} [μm]	0.05	0.032	0.032	0.05, 1.75	0.39, 1.9
std. dev.	2.0	2.0	2.0	2.03, 2.03	2.0, 2.15
hygroscopicity	hydrophilic	hydrophobic	hydrophilic	hydrophilic	hydrophobic
threshold RH	95 %	n/a	95 %	95 %	n/a

ACPD
11, 26477–26520, 2011

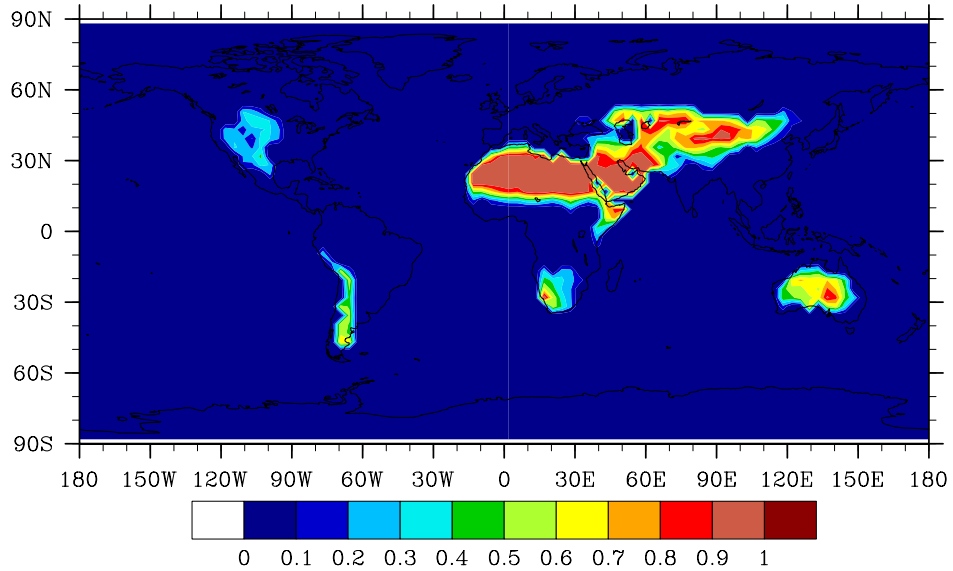

Fig. 1. An average over 12 monthly means of bare ground fraction in potential dust source regions as prescribed in CanAM4-PAM. Each monthly mean is averaged over the CTEM model results during year 1850–2005.

ACPD
11, 26477–26520, 2011

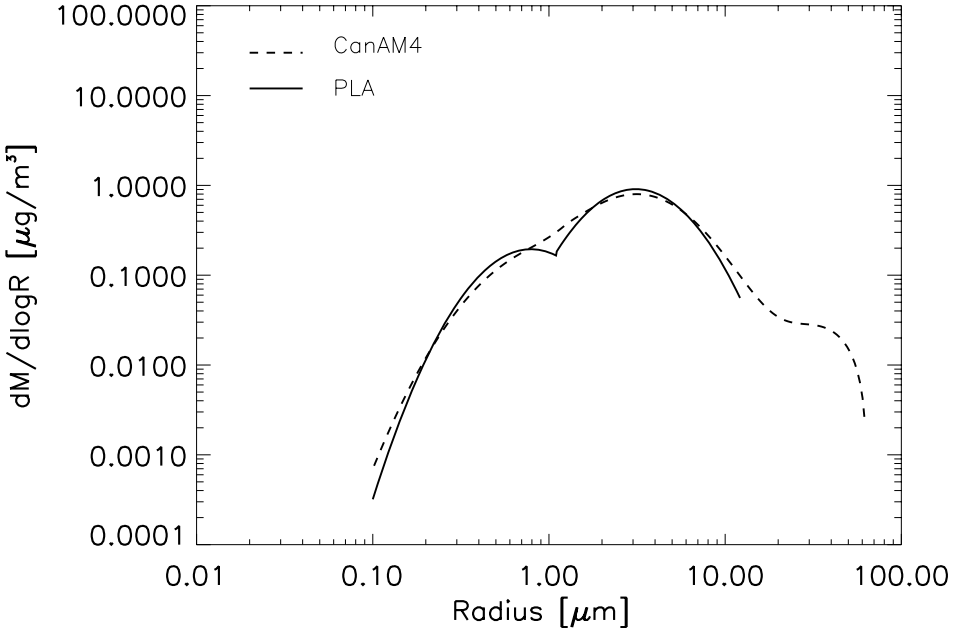

Fig. 2. Annual global mean size distribution of dust emission mass flux. The dashed line is the emitted dust flux in 192 prescribed bins in CanAM4. The solid line is a PLA distribution fitting to the parameterized dust emission, the two PLA size sections are for submicron ([0.1, 1] μm) and supermicron ([1, 10] μm) respectively.

ACPD
11, 26477–26520, 2011

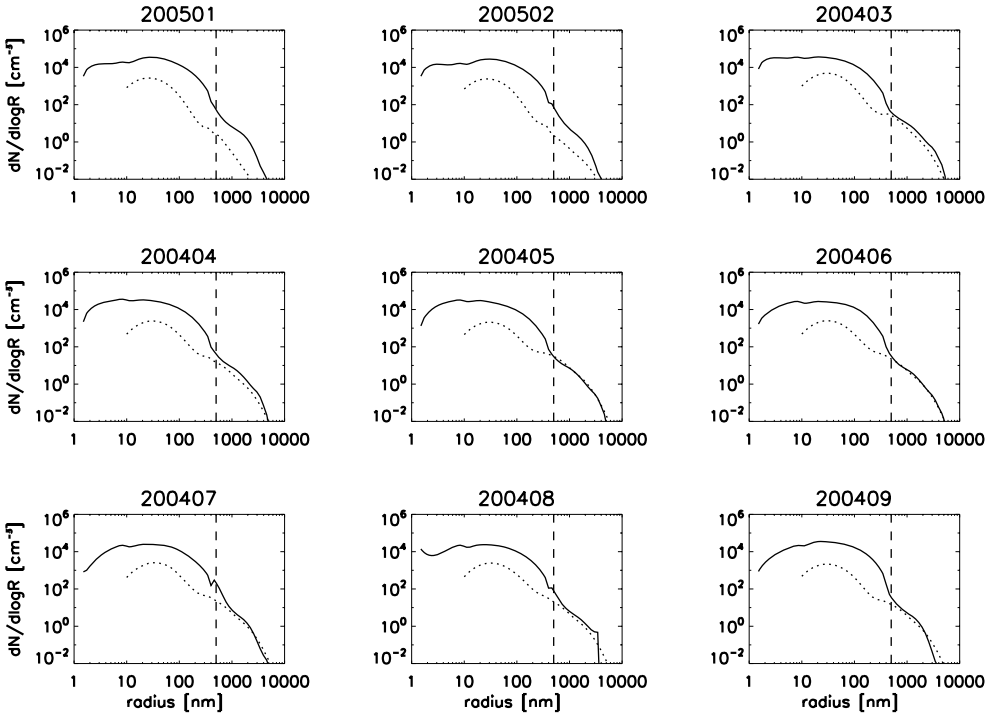

Fig. 3. Aerosol number size distribution in Beijing from March 2004 to February 2005. The solid line refers to the observations and the dotted line to the model results. The vertical dashed line is a separation between the submicron and supermicron modes.

ACPD
11, 26477–26520, 2011

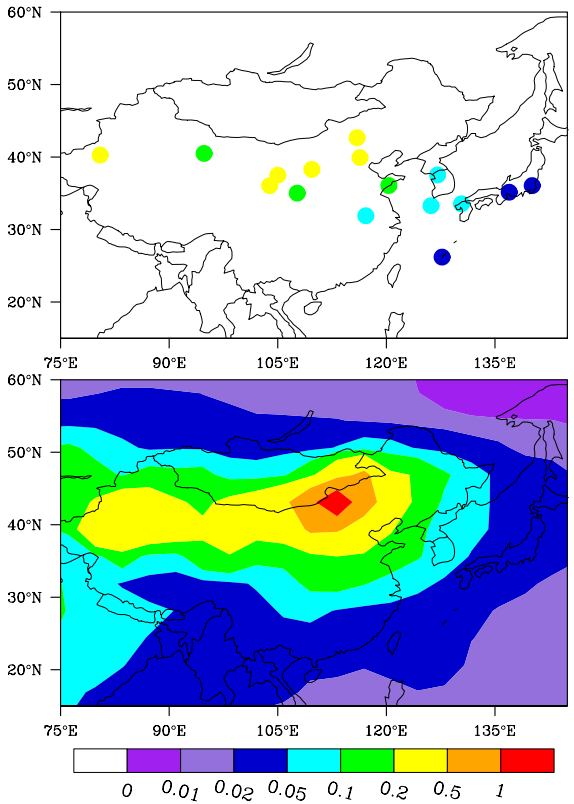

Fig. 4. Surface distribution of dust concentration (mg m^{-3}) from visibility-based estimates in 16 stations covering Asian deserts and influenced regions (top panel). Data are averaged over March, April and May (MAM) during years 2000 and 2001. CanAM4-PAM is run with nudging for 2000 and 2001. Simulation results averaged in MAM are shown in the bottom panel.

ACPD
11, 26477–26520, 2011

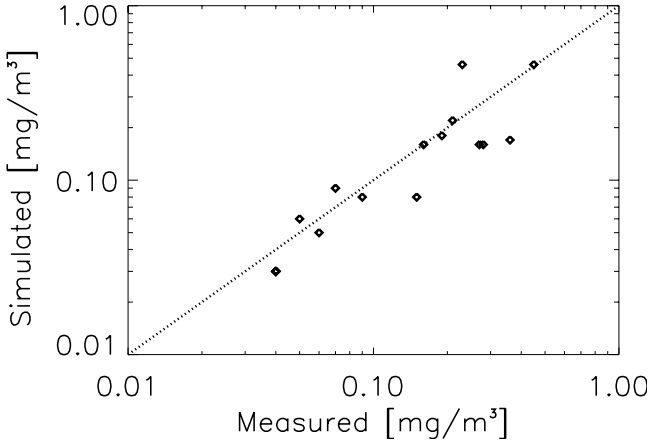

Fig. 5. Comparison of surface dust concentration between CanAM4-PAM simulation and visibility-based estimates from measurements in Asia. Data are averaged over MAM during years 2000 and 2001. Measured data are taken from 16 stations as shown in Fig. 4. Simulated data are obtained at the same locations as measurements. The dashed line is the 1:1 line.

ACPD
11, 26477–26520, 2011

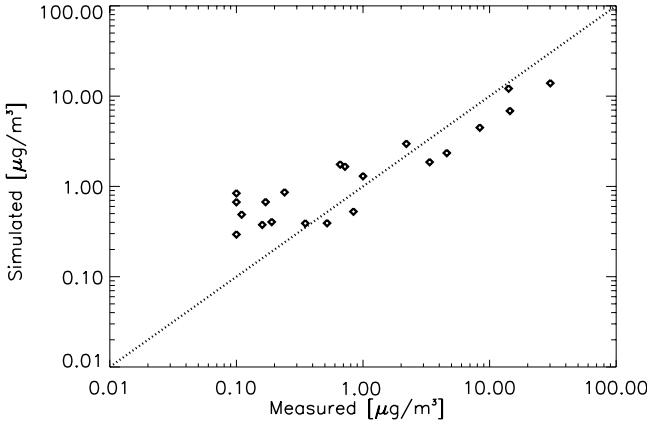

Fig. 6. Comparison of annual mean surface dust mass concentrations at 21 marine sites. Measurements are from the University of Miami (Prospero, 1999). Simulations are from a 5-yr climatology run with CanAM4-PAM. The dashed line is the 1:1 line.

ACPD
11, 26477–26520, 2011

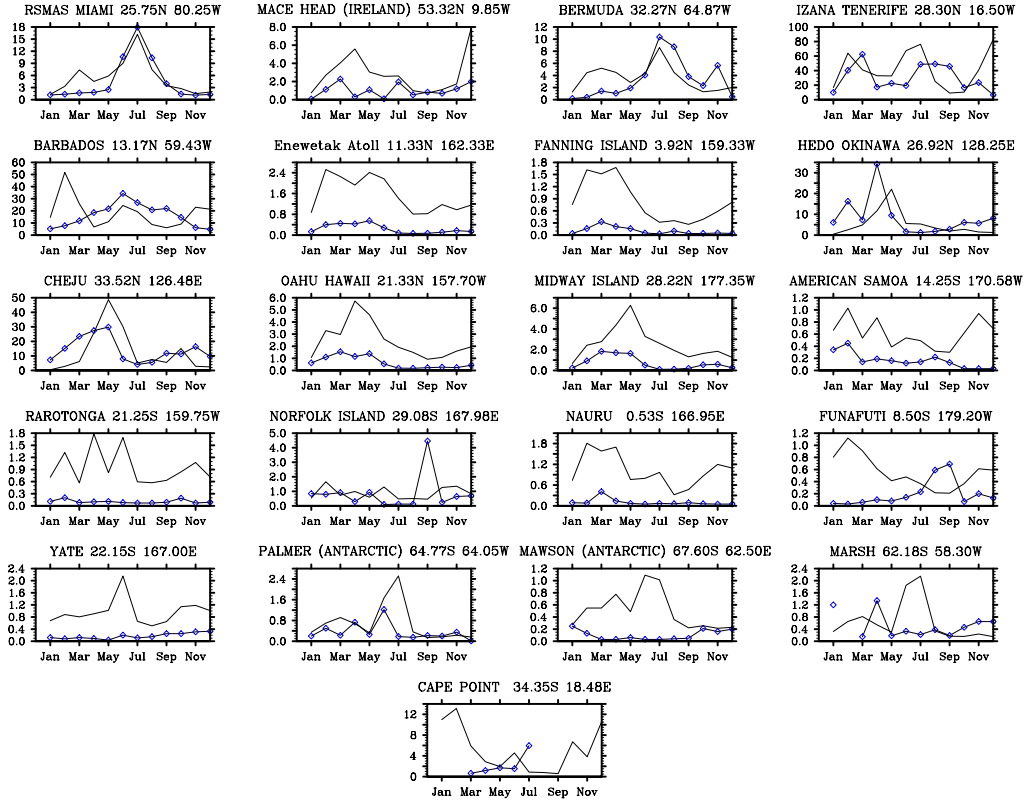

Fig. 7. Comparison for monthly mean surface dust mass concentrations [$\mu g\,m^{-3}$] at 21 marine sites. Measurements (blue line with diamonds) are taken from the network of the University of Miami (Prospero, 1999). Model results are shown in black. Note that the vertical scale is different in each panel.

ACPD
11, 26477–26520, 2011

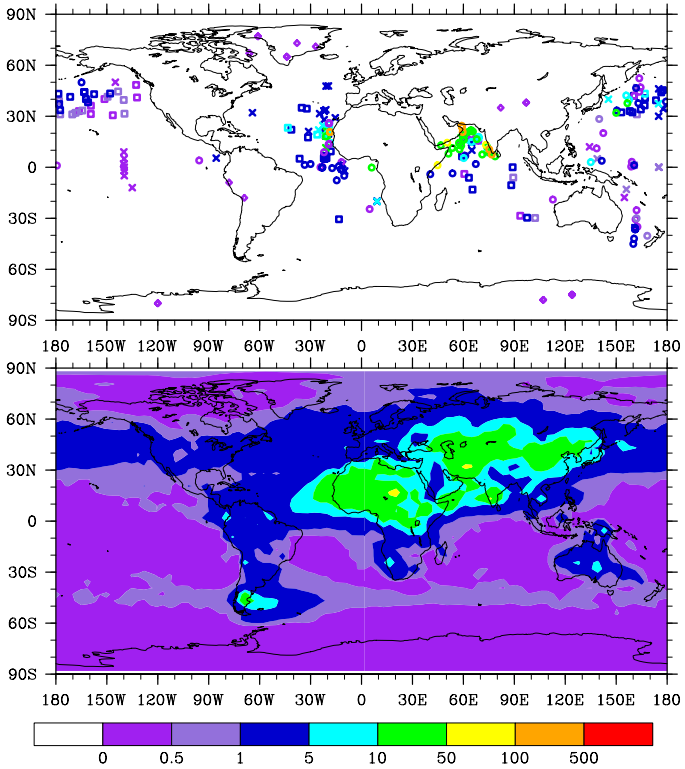

Fig. 8. Comparison between measured and modelled deposition rates of dust aerosols. The upper panel shows the collected records from DIRTMAP (Kohfeld and Harrison, 2001). Circles, squares and crosses are for marine sediment data from terrigenous fraction measurements, from trap collection and for non-carbonate accumulation rates respectively. Diamonds are for ice core records. The lower panel shows the global dust deposition rate from the climatology simulation with CanAM4-PAM. Unit: $g\,m^{-2}\,yr^{-1}$.

ACPD
11, 26477–26520, 2011

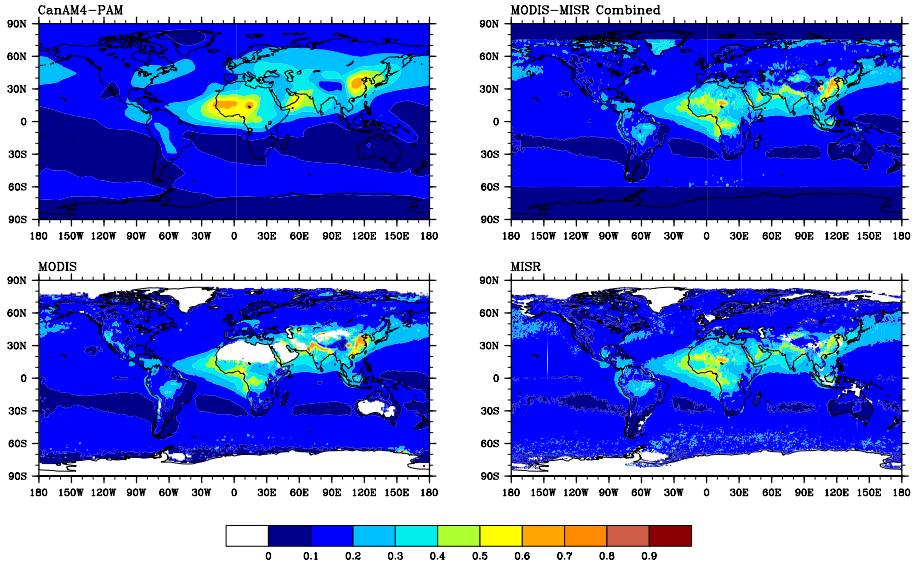

Fig. 9. Comparison between model results and satellite measurements of annual mean total aerosol optical depth (AOD) at 0.55 µm for time period 2001–2006. Results of CanAM4-PAM are from a simulation with nudging towards reanalysis (top left). Satellite retrievals from MODIS (bottom left), MISR (bottom right) and from a hybrid dataset (top right) are shown. Areas with missing values appear white.

ACPD
11, 26477–26520, 2011

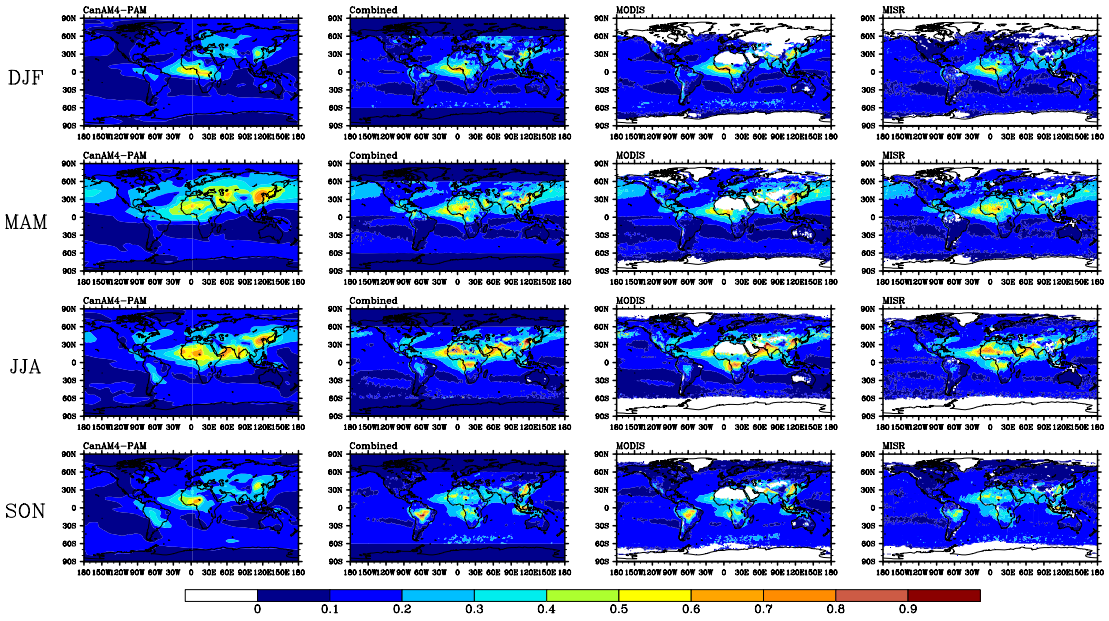

Fig. 10. Same as Fig. 9 but for seasonal means. Rows from the top to the bottom are winter (DJF), spring (MAM), summer (JJA) and autumn (SON). Columns from the left to the right are CanAM4-PAM results, combined dataset, MODIS and MISR data respectively.

ACPD
11, 26477–26520, 2011

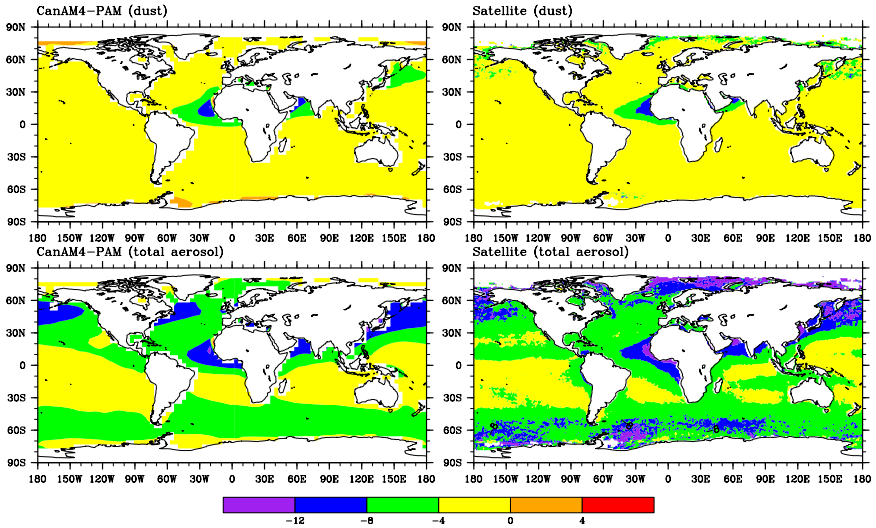

Fig. 11. ADRF comparison between satellite measurements and CanAM4-PAM results for dust and total aerosols over the ocean. Unit is W m^{-2}. Data are for year 2001.

ACPD
11, 26477–26520, 2011